RESEARCH ARTICLE

NANO · MICRO small
www.small-journal.com

# Constructing Pentagonal Topological Defects in Carbon Aerogels for Flexible Zinc-Air Batteries

*Yongfa Huang, Tingzhen Li, Runxin Huang, Kaimeng Xu, Zehong Chen, Chao Huang, Wu Yang, Youzhi Song, Zhongxin Chen, Ruidong Xia, Kasim Ocakoglu, Shimelis Admassie, Emmanuel Iwuoha, Linxin Zhong, and Xinwen Peng**

**In the context of energy conversion, the design and synthesis of high-performance metal-free carbon electrocatalysts for the oxygen reduction reaction (ORR) is crucial. Herein, a one-step nitrogen doping/extraction strategy is proposed to fabricate 3D nitrogen-doped carbon aerogels (NCA-Cl) with rich pentagonal carbon topological defects. The NCA-Cl electrocatalyst exhibits superb ORR activity, displaying a half-wave potential of 0.89 V vs RHE and 0.74 V vs RHE under alkaline (0.1 M KOH) and acidic (0.1 M $HClO_4$) media, respectively, thanks to the balanced $^*OOH$ intermediate adsorption and desorption induced by the pentagonal carbon topological defects and nitrogen dopants. The aqueous zinc-air battery (ZAB) equipped with the NCA-Cl cathode delivers a peak power density of 206.6 mW $cm^{-2}$, a specific capacity of 810.6 mAh $g^{-1}$, and a durability of 400 h, and the flexible ZAB also performed convincingly. This work provides an effective strategy for the formation of topological carbon defects for the enhancement of the electrocatalytic activity of carbon-based catalysts.**

## 1. Introduction

Zinc-air batteries (ZAB) are considered a promising, environmentally friendly, and sustainable energy conversion technology due to their high theoretical energy density (1086 Wh $kg^{-1}$), environmental friendliness, and abundant zinc resources.[1] However, the slow kinetics of the 4-electron oxygen reduction reaction (ORR) occurring on the cathode catalyst severely limits the wide application of ZAB.[2] Although Pt-based nanomaterials are the most practical catalysts for ORR, the scarcity, high price, and poor durability of Pt greatly affect their large-scale application. Presently, atomically dispersed transition metals with high activity are considered the most promising Pt-free catalysts.[3] Nevertheless, their durability level is still unsatisfactory due to the dissolution of active metal sites caused by oxidative $H_2O_2$ attack or oxidative corrosion of carbon carriers.[4] In addition, since ZAB involves a gas-liquid-solid three-phase reaction, it generates a large number of gas bubbles during prolonged cycling. These bubbles can impact the catalyst adhered by the binder leading to catalyst detachment from the substrate and ultimately leading to a decrease in ZAB stability. Therefore, there is an urgent need to develop highly active and robust metal-free one-piece catalysts.

Carbon nanomaterials (CNMs) have become the foremost alternative to noble metal-based materials as ORR and OER electrocatalysts given their low cost, high structural tunability, and good stability.[5] However, carbon itself has a symmetric, locally

Y. Huang, T. Li, R. Huang, Z. Chen, C. Huang, W. Yang, Y. Song, L. Zhong, X. Peng
School of Light Industry and Engineering
South China University of Technology
Guangzhou 510641, China
E-mail: fexwpeng@scut.edu.cn

K. Xu
Yunnan Provincial Key Laboratory of Wood Adhesives and Glued Products, International Joint Research Center for Biomass Materials
Southwest Forestry University
Kunming 650224, China

Z. Chen
School of Science and Engineering
The Chinese University of Hong Kong
Shenzhen, Guangdong 518172, China

The ORCID identification number(s) for the author(s) of this article can be found under https://doi.org/10.1002/smll.202502067

DOI: 10.1002/smll.202502067

R. Xia
State Key Laboratory of Organic Electronics and Information Displays & Institute of Advanced Materials (IAM)
School of Materials Science and Engineering
Nanjing University of Posts & Telecommunications
Nanjing 210023, China

K. Ocakoglu
Department of Engineering Fundamental Sciences, Faculty of Engineering
Tarsus University
Tarsus 33400, Turkey

S. Admassie
Department of Chemistry
Addis Ababa University
Addis Ababa PO BOX 1176, Ethiopia

E. Iwuoha
SensorLab (UWC Sensor Laboratories)
Department of Chemistry
University of the Western Cape
Bellville, Cape Town 7535, South Africa

 

$sp^2$-hybridized electronic structure and therefore performs poorly in electrocatalysis. The introduction of heteroatoms (especially N-doping) into CNMs is an effective strategy to activate electron donors or acceptors in different reaction states by altering the asymmetric distribution of electron conjugate structures in carbon materials to achieve favorable band gaps, electronic structures, and density of states.[6] In addition, the introduction of carbon defects (including vacancy defects, topological defects (e.g., pentagonal, heptagonal, octagonal, etc.), and edge defects) into the carbon structure has been widely exploited to enhance catalytic activity by directly providing adsorption sites or modifying electronic properties.[7] Nevertheless, the lack of sufficient active sites participating in ORR has resulted in the catalytic efficiency of the aforementioned two types of active sites remaining incomparable with that of the current benchmark electrocatalysts. In light of the aforementioned considerations, it can be posited that the fabrication of "desirable" catalytically active sites through the utilization of defect and doping engineering strategies, which entail the combination of carbon defects (including pentagons, vacancies, and edges) and heteroatom doping, will synergistically enhance the electrocatalytic performance.

Flexible and compressible carbon aerogels prepared from oriented freeze-dried cellulose nanofibres (CNFs) are excellent one-piece functional carbon materials with high specific surface area, low density, high electrical conductivity, and good compressibility, which make them show unique structural advantages when used in three-phase catalytic reactions.[8] Among many CNFs, 2,2,6,6-tetramethylpiperidinyl-1-oxide (TEMPO) oxidized cellulose nanofibers (TOCNs) have excellent mechanical properties of carbon aerogels prepared from them due to their high crystallinity, uniform width (3–4 nm), and high aspect ratio and their ability to be completely dispersed as single fibers in water.[9] Nonetheless, the catalytic activity of carbon aerogels directly subjected to pyrolysis is not satisfactory. Therefore, it is foreseen that the construction of "desirable" active sites on carbon aerogels can well solve the problem of the stability of ZAB.

In this work, nitrogen-doped carbon aerogel electrocatalysts enriched with pentagonal defects (NCA-Cl) were designed and fabricated via a one-step nitrogen doping/extraction strategy. The formation of pentagonal carbon defects can be attributed to two primary factors. On the one hand, at temperatures between 550 and 725 °C, the nitrogen in nitrogen-doped carbon collides with $NH_3$, resulting in the release of HCN. This subsequently leads to carbon rearrangement, which gives rise to the formation of pentagonal defects. Alternatively, the nitrogen atoms in the nitrogen-doped carbon will be released as $NH_3$ under pyrolysis, and the unsaturated carbon will undergo rearrangement to form carbon defects. The result is an NCA-Cl catalyst with "desirable" catalytic activity sites, and a unique electronic structure that facilitates the adsorption/desorption of oxygen intermediates, thus accelerating the reaction kinetics and providing excellent ORR/OER activity under alkaline conditions. Furthermore, it exhibits comparable ORR activity to that of commercial Pt/C under acidic conditions. These findings, in conjunction with the encouraging performance in ZABs, indicate that the NCA-Cl electrocatalyst is one of the most advanced carbon-based metal-free bifunctional oxygen electrocatalysts to date.

## 2. Results and Discussion

### 2.1. Morphology and Structure of NCA-Cl

Since the carbonization temperature is crucial for the electrocatalytic performance, we optimized the pyrolysis temperature to determine the optimal conditions. Physical characterization by X-ray diffraction (XRD), X-ray photoelectron spectroscopy (XPS), Raman, Brunauer-Emmett-Teller (BET), and X-ray absorption spectroscopy (XAS) showed that maintaining at 900 °C for 2 h could yield products with abundant micro-mesopores, high nitrogen doping, high defect density, and high electrical conductivity, providing a foundation for subsequent studies (Figures S1–S6, Supporting Information). In addition, we further optimized the ratios of CNF and $g\text{-}C_3N_4$ (the mass ratios of CNF to $g\text{-}C_3N_4$ were 1:0.5, 1:1, 1:2, 1:3, and 1:5). As shown in Figure S7 (Supporting Information), the NCA catalyst exhibited a more positive half-wave potential when the ratio of CNF to $g\text{-}C_3N_4$ was 1:3, which indicated that NCA had a superior oxygen reduction activity. To illustrate the superiority of the "one-step nitrogen doping/removal" strategy for the fabrication of pentagonal carbon defects coupled with nitrogen-doped CNF-derived carbon aerogels, we systematically investigated four catalysts, namely, CA (CNF-derived carbon aerogels), CA-Cl (low-temperature nitrogen-doped CNF-derived carbon aerogels), NCA (high-temperature nitrogen-doped/removed CNF-derived carbon aerogels) and NCA-Cl (one-step low-temperature nitrogen-doped high-temperature nitrogen-removed CNF-derived carbon aerogels). NCA-Cl was prepared by a process of "one-step nitrogen doping/extraction", as illustrated in **Figures 1a** and S8 (Supporting Information). First, CNF and $g\text{-}C_3N_4$ were dispersed homogeneously by van der Waals self-assembly. This dispersion remained stable for over a month, indicating uniform dispersion of $g\text{-}C_3N_4$ in CNF (Figure S9, Supporting Information). Subsequently, CNF-based aerogels were prepared by directional freeze-drying.[9a,10] The successful dispersion of $g\text{-}C_3N_4$ in CNF was additionally corroborated by solid-state nuclear magnetic resonance spectroscopy (NMR) (Figure S10, Supporting Information).[11] Finally, NCA-Cl was prepared by one-step pyrolysis.

As illustrated in Figure 1c, the scanning electron microscopy (SEM) image reveals that the porous carbon nanosheets in NCA-Cl interconnect to form a 3D honeycomb architecture. The carbon sheets exhibit a substantial pore size, with radii between 10 and 20 μm, and a high density of nanopores. The formation of the large pores can be attributed to ice crystal sublimation, while the nanopores are primarily the result of $NH_3$ etching. The micro-CT images (Figure 1b) further corroborate that NCA-Cl has a 3D honeycomb layered structure. Interestingly, high-temperature nitrogen extraction gives the material richer micro/mesopores, while low-temperature nitrogen doping reduces the specific surface area of the material (Figure S11, Supporting Information). Furthermore, the honeycomb structure of NCA-Cl enables compressibility and flexibility (Figure S12, Supporting Information). The nanosheet surface of CA after freeze-drying and pyrolysis of CNF only is notably smooth, further illustrating the efficacy of the one-step method employed to fabricate the nanoporous structure (Figure S13, Supporting Information). Figure S14 (Supporting Information) illustrates the transmission electron microscopy (TEM) images of NCA-Cl and CA-Cl. The images show

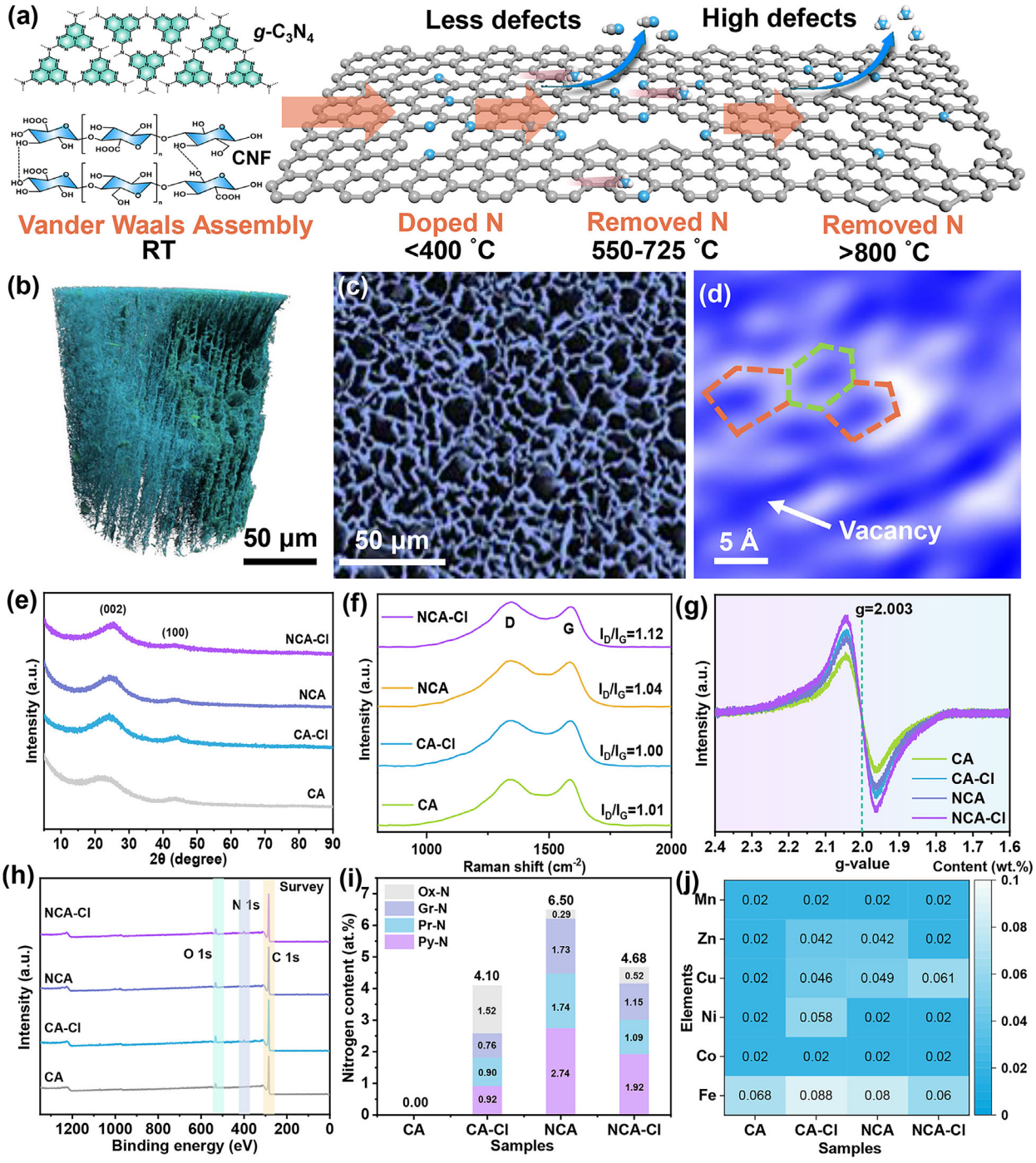


**Figure 1.** Schematic of the microstructure and possible pyrolysis process of NCA-Cl. a) Scheme of possible formation processes of carbon defects. b) Micro-CT image of NCA-Cl. c) SEM images of NCA-Cl. d) ACTEM image of NCA-Cl after FFT. e) XRD patterns, Raman spectra f), and EPR spectra g) of CA, CA-Cl, NCA, and NCA-Cl samples. XPS spectra h), Nitrogen content and relative content of each N-specie i), and ICP-OES j) of CA, CA-Cl, NCA, and NCA-Cl.

that NCA-Cl has a higher microporosity density and a more disordered graphite structure compared to CA-Cl, indicating that high-temperature nitrogen extraction is more favorable for the preparation of high-density defect carbon materials. Figure 1d and Figure S15 (Supporting Information) illustrate aberration-corrected transmission electron microscopy (AC-TEM) images of NCA-Cl. Figure S15 (Supporting Information) depicts numerous topological and vacancy defects in NCA-Cl. The fast Fourier transform (FFT)-filtered image (Figure 1d) of the labeled region in Figure S15 (Supporting Information) reveals carbon vacancies

adjacent to pentagonal carbon defects (orange line) and hexagonal carbon (green line). These findings confirm the effectiveness of the "one-step nitrogen doping/removal" method in preparing pentagonal topological defects.

The XRD patterns of CA, CA-Cl, NCA, and NCA-Cl (Figure 1e) exhibit two broad peaks, corresponding to the graphitic carbon (002) and (100) planes at $2\theta = 23.1°$ and 43.9°, respectively. In contrast, the diffraction peak of NCA-Cl is considerably weaker, indicating that NCA-Cl is a more disordered and defective material. Correspondingly, the Raman spectra of CA, CA-Cl, NCA, and NCA-Cl exhibit peaks at 1348 $cm^{-1}$ (D-band) and 1588 $cm^{-1}$ (G-band) (Figure 1f). These peaks are indicative of $sp^3$-deficient carbon and $sp^2$-mixed aromatic structures, respectively, which are associated with disordered and graphitized carbon structures.[12] The NCA-Cl sample shows the largest $I_D/I_G$ ratio, again suggesting that the doped/removed strategy for synthesizing highly amorphous, defective carbon materials is highly effective. The $I_D/I_G$ ratio fluctuates with N doping content, particularly when N-doped impurity defects are prevalent in the carbon matrix.[13] Despite the higher nitrogen content in NCA compared to NCA-Cl (Figure S16, Table S1, Supporting Information), the $I_D/I_G$ ratio of NCA-Cl remains larger, indicating a higher defect density in NCA-Cl compared to NCA. The results were further confirmed by electron paramagnetic resonance (EPR), as shown in Figure 1g, where NCA-Cl exhibits the peak signal with the highest intensity at a magnetic field strength of 2.003 G, indicating a higher defect density in NCA-Cl.[14] Furthermore, to provide additional evidence that the materials are free of metals, XPS and inductively coupled plasma optical emission spectrometer (ICP-OES) tests were conducted on the materials. Figure 1h presents the complete XPS spectrum, which reveals that the synthesized material comprises solely three elements: carbon (C), nitrogen (N), and oxygen (O). Furthermore, the XPS spectrum demonstrates that the synthesized material lacks metallic impurities. Among the materials, NCA exhibits the highest nitrogen content (6.50%) (Figure 1i). The inductively coupled plasma optical emission spectrometer (ICP-OES) tests confirmed that the material is a metal-free catalyst. The presence of Fe, Co, Ni, Cu, Mn, and Zn with high activity is below 0.1 wt.% in the synthesized material and can be disregarded in ORR active site confirmation (Figure 1j). These experimental results strongly support the feasibility of the proposed approach for fabricating high-density defective carbon materials.

### 2.2. The Formation Process of High-Density Carbon Defects in NCA-Cl

The formation process of carbon defects in NCA-Cl samples was investigated using both *in-situ* and *ex-situ* techniques. The XRD patterns at various temperatures are shown in **Figure 2a**. As shown in Figure 2a, when the temperature reaches 200 °C, the (200) diffraction peak of CNF is still detectable, indicating that the crystal structure of CNF is preserved. However, as the temperature increases to 400 °C, the (200) diffraction peak of CNF disappears, indicating the complete decomposition of CNF,[15] which aligns with the CNF thermogravimetric curve (Figure S17, Supporting Information). The intensity of the (002) diffraction peak of $g$-$C_3N_4$ initially increases, then decreases, and eventually disappears as the temperature rises, suggesting that in the early stages of heating (<400 °C), the molecular chains of $g$-$C_3N_4$ may undergo rearrangement and ordering due to thermal energy, promoting layer stacking and increased order. This results in a higher intensity of the (002) diffraction peak, indicating increased crystallinity of $g$-$C_3N_4$. When the temperature is further increased (400–600 °C), $g$-$C_3N_4$ reaches its thermal stability limit and begins pyrolysis and decomposition, weakening its ordered structure and decreasing crystallinity, which reduces the intensity of the (002) diffraction peak. At high temperatures (≈600 °C), $g$-$C_3N_4$ loses its crystalline structure entirely, transforming into an amorphous or other disordered structure, causing the (002) peak to disappear, as amorphous materials lack the long-range order needed for distinct diffraction peaks in XRD analysis. Above 650 °C, $g$-$C_3N_4$ further decomposes into gaseous products such as $NH_3$ and HCN, resulting in a complete structural breakdown. With the full decomposition of $g$-$C_3N_4$, the (002) diffraction peak characteristic of graphite becomes visible, and this peak intensifies with increasing temperature, indicating greater graphitization. The infrared (IR) spectra at different temperatures are shown in Figure 2b. The N—H bond ≈3200 $cm^{-1}$ disappears above 400 °C, indicating a reduction in defect structures in $g$-$C_3N_4$, including nitrogen or carbon vacancies and hydrogen bonding defects, which is consistent with the XRD results across these temperatures.[16] When the temperature exceeds 600 °C, the characteristic C—N—C bond of $g$-$C_3N_4$ vanishes, further confirming the decomposition of $g$-$C_3N_4$, and nitrogen- and oxygen-containing functional groups gradually diminish.[17] Additionally, the XPS results (Figure 2c; Figure S18, Table S2, Supporting Information) at various temperatures confirm the temperature dependence of different nitrogen-containing components (Py-N (398.5 and 398.1 eV), Pr-N (399.2 and 399.7 eV), Gr-N (401.1 eV), and Ox-N (402.9 eV)).[18] The nitrogen content decreases most up to 200 °C, mainly due to the decomposition of CNF. As the temperature increases to 600 °C, nitrogen content rises, mainly due to $NH_3$ released from $NH_4Cl$ decomposition, which etches and dopes the carbon network. The peak fitting results for N1s further revealed that an increase was observed only in the Py-N content, indicating that the low-temperature gasification doping method primarily introduces nitrogen atoms into the carbon lattice in the form of Py-N. When the temperature exceeds 600 °C, the Gr-N content initially increases and then gradually decreases, suggesting that some nitrogen atoms remain in the carbon lattice as graphitic nitrogen following the complete decomposition of $g$-$C_3N_4$. Notably, the significant decrease in Py-N and Pr-N content between 600 and 700 °C can be attributed partly to the complete decomposition of $g$-$C_3N_4$ and may also be related to the formation of carbon defects.

We further explored the gaseous products released during pyrolysis using thermogravimetric infrared mass spectrometry (TG-IR-MS) to ascertain potential causes for carbon defect formation. To simulate the nitrogen doping process at low temperatures, 5 wt% ammonium chloride was incorporated into the experiment. As shown in Figure 2d, the in situ IR spectrograms tracked oxygen-containing substances and bonds ($CO_2$, C—O, and O—H), nitrogen-containing bonds (N—H and C≡N), and C—H bonds.[19] The IR signals are mainly ≈550–725 °C. The IR signals are weak at low temperatures owing to the low intensity of the products released from the low content of CNF and

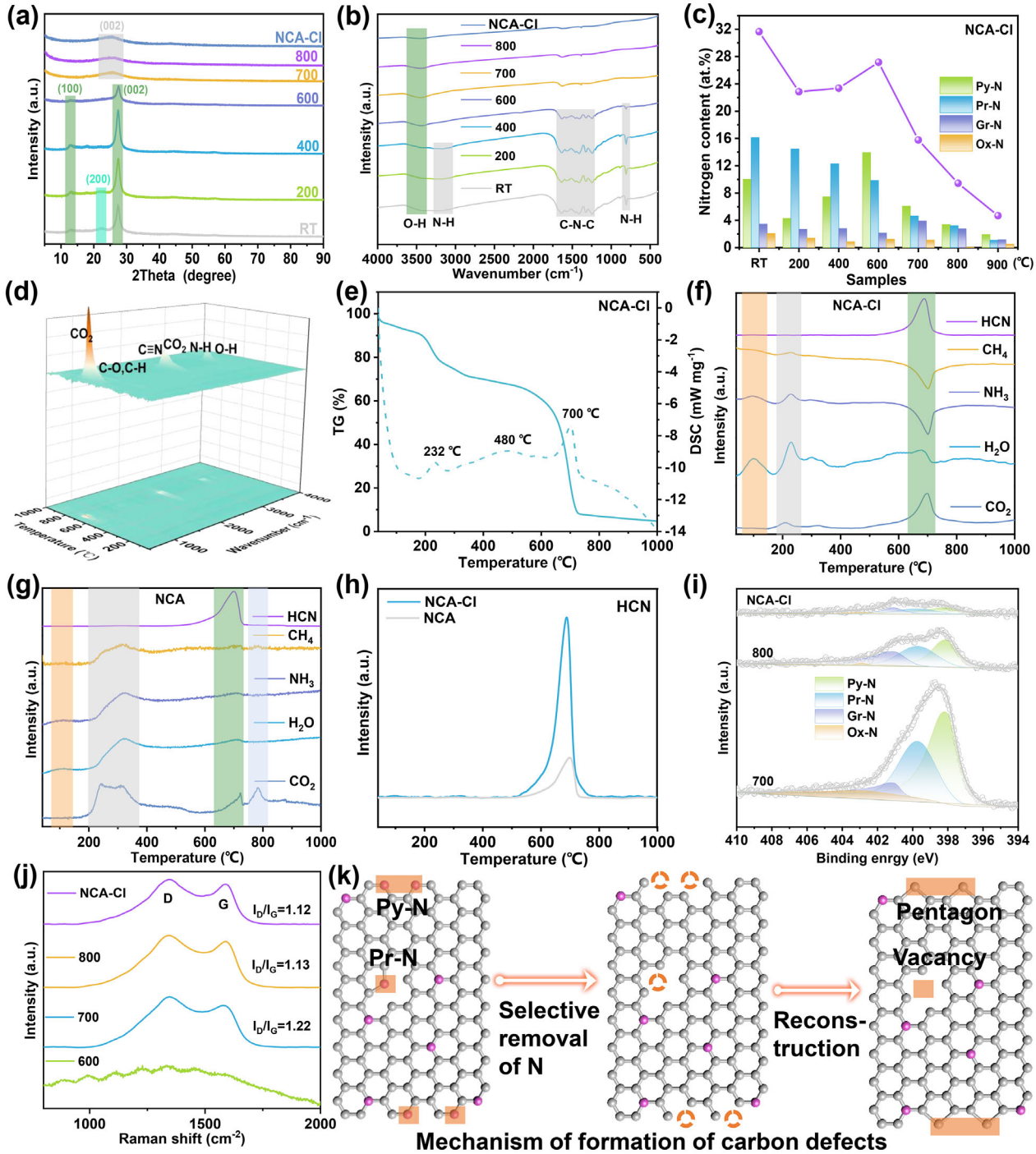


**Figure 2.** Mechanism of formation of pentagonal defects in NCA-Cl. The XRD patterns a), IR spectra b), and configurations of N dopants c) of NCA-Cl at different temperatures. TG-IR-MS analysis d–f) of gases evolved from the thermal degradation of NCA-Cl. TG-MS analysis g) of gases evolved from the thermal degradation of NCA. MS analysis h) of gases evolved from the thermal degradation of NCA and NCA-Cl. i) The high-resolution N 1s XPS spectra of NCA-Cl at different temperatures. j) Raman spectra of NCA-Cl at different temperatures. k) Schematic diagram of carbon defect formation.

$NH_4Cl$. The thermogravimetric curves (Figure 2e) exhibit three broad peaks corresponding to the decomposition processes of the components at ≈232 °C (dominated by CNF and ammonium chloride decomposition), 480 °C (primarily $g$-$C_3N_4$ rearrangement and ordering), and 700 °C (mainly $g$-$C_3N_4$ decomposition). Additionally, the thermogravimetric infrared curves of CNF@$g$-$C_3N_4$ indicate differing decomposition temperatures for the two components (Figure S19, Supporting Information). The variation in gaseous products (such as HCN, $CH_4$, $NH_3$, $H_2O$, and $CO_2$) with temperature is illustrated by the mass spectra presented in

Figure 2f, g. Peaks for $H_2O$, $CO_2$, $CH_4$, and $NH_3$ ≈200 °C correspond to CNF and ammonium chloride decomposition, corroborating XRD, IR, and XPS results. HCN, $H_2O$, and $CO_2$ exhibit peaks ≈625–725 °C, indicating *g*-$C_3N_4$ decomposition and significant deoxygenation reactions. Interestingly, the profiles of $CH_4$ and $NH_3$ for the NCA-Cl sample display inverse peaks, whereas the NCA sample exhibits positive peaks, with the HCN profile of the NCA-Cl sample showing a larger peak area (Figure 2h). These intriguing results suggest that $NH_3$ removes Py-N and Pr-N, subsequently releasing them as HCN. Furthermore, the activated carbon undergoes rearrangement, leading to the formation of carbon defects, including topological or vacancy defects. Figure 2j shows the Raman spectra at varying temperatures. The D/G peak of carbon is influenced by the intense fluorescence of undecomposed *g*-$C_3N_4$ at 600 °C. The $I_D/I_G$ value decreases as temperature increases, due to the significant impact of nitrogen content on the $I_D/I_G$ ratio, resulting in a marked reduction in the $I_D/I_G$ value between 700 and 800 °C. The $I_D/I_G$ values at 800 and 900 °C are comparable, indicating that the removal of Py-N and Pr-N enhances the $sp^2$ hybridization of carbon. Figure 2i illustrates the XPS N1s peak fitting results at varying temperatures. The rapid decline in nitrogen content (or four distinct fractions) with increasing temperature is attributable to the elimination of nitrogen atoms in the form of ammonia as a consequence of pyrolysis, as evidenced in Figure 2f. This is also consistent with the recently reported mechanism for the formation of carbon defects.

In light of these results, a proposed process for carbon defect formation is as follows (Figures 1a and 2k): Initially, $NH_4Cl$ decomposes into $NH_3$ and HCl between 225 and 600 °C, with decomposed ammonia etching CNF-derived carbon to create nitrogen-doped carbon. Subsequently, ammonia gas released from *g*-$C_3N_4$ decomposition (625–725 °C) bombards Py-N and Pr-N in the carbon lattice, leading to Pr-N and Py-N removal and the formation of HCN and $CH_4$ (from demethylation during pyrolysis). The surrounding unsaturated activated carbon undergoes rearrangement, resulting in carbon defects, such as vacancies and pentagonal topological structures. Pr-N is more likely to form vacancy defects, while Py-N predominantly results in pentagonal topological defect structures. Ultimately, at temperatures exceeding 725 °C, further nitrogen removal due to enhanced pyrolysis results in increased high-density carbon defects.

### 2.3. Electrochemical ORR Performance

To demonstrate the effectiveness of the "one-step nitrogen doping/removal" strategy for preparing high-density carbon defects and to examine the impact of defect densities on ORR performance, we measured the ORR/OER performance of NCA-Cl using a rotating disc electrode (RDE), rotating ring-disc electrode (RRDE), and a three-electrode system in $O_2$-saturated 0.1 M KOH.[20] Figure S20 (Supporting Information) presents the ORR activity of samples prepared at varying temperatures. NCA-900 exhibits a more positive half-wave potential, indicating that a calcination temperature of 900 °C is optimal, consistent with previous physical characterization results. The oxygen reduction peak of NCA-Cl appeared at 0.89 V (vs RHE), higher than that of CA (0.73 V vs RHE), CA-Cl (0.83 V vs RHE), and NCA (0.84 V vs RHE), suggesting superior ORR performance for NCA-Cl (Figure S21, Supporting Information). Linear scanning voltammetry (LSV) curves (**Figure 3a**) show that the NCA-Cl catalyst ($E_{onset}$ = 1.01 V vs RHE, $E_{1/2}$ = 0.89 V vs RHE) exhibited ORR activity superior to the commercial Pt/C sample and other controls, as illustrated in Figure 3a,b. These findings suggest that increasing carbon defect density through the "one-step nitrogen doping/removal" approach significantly enhances ORR activity.

As illustrated in Figure 3c, NCA-Cl exhibited the highest kinetic current densities at 0.75 V (24.39 mA $cm^{-2}$), 0.8 V (20.45 mA $cm^{-2}$), and 0.85 V (7.69 mA $cm^{-2}$), respectively, surpassing CA, CA-Cl, NCA, and Pt/C catalysts. As illustrated in Figure 3d, NCA-Cl exhibits the lowest Tafel slope (71.1 mV $dec^{-1}$), which is considerably lower than that of the control samples and commercial Pt/C. This further suggests that the high-density carbon-defected NCA-Cl can provide smaller energy barriers and faster ORR kinetics. The Koutecky–Levich (K-L) plot (Figure 3e) shows an electron transfer number ≈4, suggesting that NCA-Cl facilitates a direct four-electron pathway from $O_2$ to $OH^-$. Furthermore, RRDE measurements (Figure 3f) indicated an electron transfer number above 3.7, with $H_2O_2$ yield remaining below 15% over a potential range of 0.2–0.8 V, confirming that NCA-Cl catalyzes a four-electron reaction. The durability of NCA-Cl was demonstrated by i-t measurements (Figure 3g). The results demonstrate that the current density retention of NCA-Cl (95.3%) is markedly superior to that of the commercial Pt/C (80.7%). The Raman spectra of the NCA-Cl catalyst after the stability test showed that the $I_D/I_G$ ratio remained at 1.12, indicating that the defective structure of NCA-Cl was not severely damaged after a long period of operation (Figure S22, Supporting Information). The decrease in pyridine nitrogen content and the increase in pyrrole nitrogen content in the N1s spectrum fitted after the stability test suggest that the pentagonal topological defect structure of the NCA-Cl catalyst may be the active site (Figure S23, Supporting Information). Additionally, the electrocatalytic OER performance of NCA-Cl proved excellent. NCA-Cl exhibited a low overpotential ($\eta$) of 371 mV at 10 mA $cm^{-2}$, comparable to $RuO_2$ (358 mV) and superior to other controls (Figure 3h). The bifunctional oxygen electrocatalytic activity of NCA-Cl was evaluated by measuring the potential difference ($\Delta E$) between $E_{j=10}$ at OER and $E_{1/2}$ at ORR. As shown in Figure 3i, the $\Delta E$ of NCA-Cl is 0.71 V, placing it among the most favorable bifunctional activities reported for carbon-based metal-free electrocatalysts, which further substantiates the superiority of the one-step nitrogen doping/removal strategy for preparing high-activity carbon-based metal-free electrocatalysts.[6b,c,21]

The electrocatalytic oxygen reduction reaction (ORR) performance of NCA-Cl under acidic media (oxygen saturated with 0.1 M $HClO_4$) was further examined.[22] The NCA-Cl catalyst demonstrated a more positive oxygen reduction peak, indicating superior ORR performance (Figure S24, Supporting Information). As illustrated in **Figure 4a,b**, the $E_{onset}$ and $E_{1/2}$ of NCA-Cl were 0.84 and 0.74 V vs RHE, respectively, which are comparable to those of standard Pt/C ($E_{onset}$ = 0.90 V vs RHE, $E_{1/2}$ = 0.76 V vs RHE) and exhibited superior performance compared to the other controls. Figure 4c illustrates that NCA-Cl exhibited high $J_k$ values at 0.65 V, 0.70 V, and 0.75 V vs RHE, comparable to those of commercial Pt/C. The superior ORR kinetics of NCA-Cl is demonstrated by its smallest tafel slope (57.7 mV $dec^{-1}$) compared to other controls and commercial

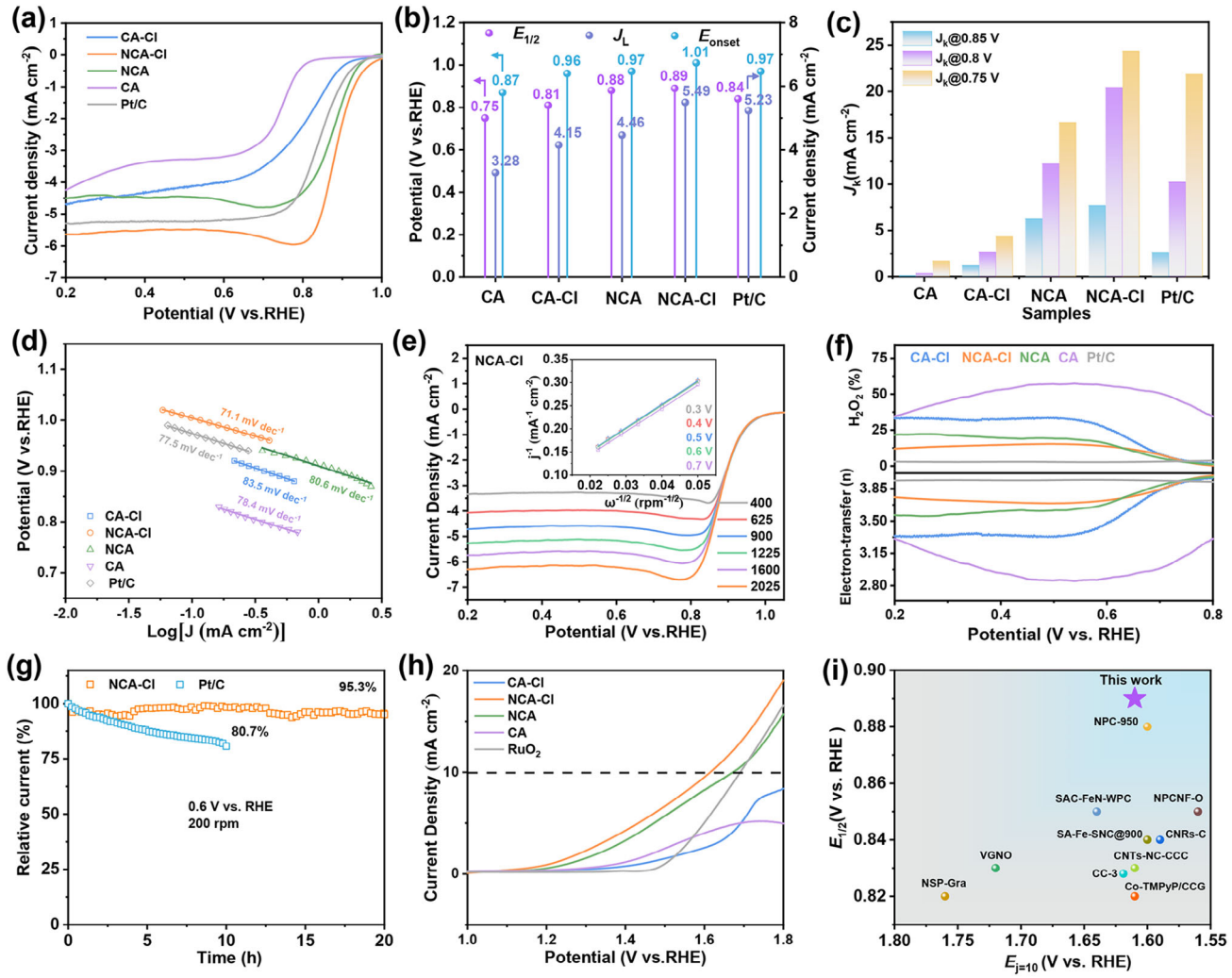


**Figure 3.** ORR and OER activity of NCA-Cl in 0.1 M KOH. a) LSV curves. b) $E_{onset}$, $E_{1/2,}$ and $J_L$ values. c)$J_K$ values. d) Tafel plots. e) LSV curves and corresponding K-L curves. f) Electron transfer number and $H_2O_2$ peroxide yield. g) The durability of the NCA-Cl catalyst and Pt/C for ORR. h) RDE polarization curves for OER. i) $\triangle E$ of samples for bifunctional electrocatalytic activity.

Pt/C (Figure 4d). Additionally, NCA-Cl showed a higher $C_{dl}$ value (45.76 mF $cm^{-2}$) (Figure 4e; Figure S25, Supporting Information), indicating a larger electrochemically active area.[23] The electron transfer number of NCA-Cl is close to 4 (Figure 4f), confirming its highly selective four-electron ORR pathway to $H_2O$, in agreement with the RRDE results in Figure 4g. In contrast, the other samples showed reduced selectivity for the four-electron pathway. The current density of NCA-Cl remained at 90.3%, significantly exceeding that of commercial Pt/C (≈81.0%) after maintaining 0.5 V vs RHE continuously for 20 h. The electrochemical impedance spectra (EIS) offer insights into catalyst kinetics and mass transfer properties. The fitted model is presented in Figure 4i and Table S3 (Supporting Information). The $R_{ct}$ corresponds to charge transfer at the electrode interface, while $R_s$ represents solution resistance. $R_{ct}$ was lowest for NCA-Cl, indicating more efficient electron transfer and faster ORR kinetics for NCA-Cl.[24] These results demonstrate the efficient ORR performance of the NCA-Cl electrocatalyst. These findings provide further evidence that nitrogen-doped coupled high-density carbon defects can dramatically enhance the activity and stability of ORR and OER, thus allowing this "desirable" catalyst to surpass the performance of most metal-free doped carbon catalysts.

### 2.4. Performance of ZABs

Considering their optimal ORR/OER performance, an aqueous rechargeable ZAB based on NCA-Cl was developed (Figure S26, Supporting Information). The assembled ZABs exhibited minimal voltage drop during galvanostatic discharge measurements across current densities ranging from 2 to 40 mA $cm^{-2}$ (**Figure 5a**), indicating excellent rate performance. When the current density was reduced to 2 mA $cm^{-2}$, the discharge was reversibly recovered. Figure 5b shows the full-discharge curves at 5 and 10 mA $cm^{-2}$. The assembled ZABs demonstrated a specific capacity of 810.6 mAh $g^{-1}$ and an energy density of 993.8 Wh $kg^{-1}$

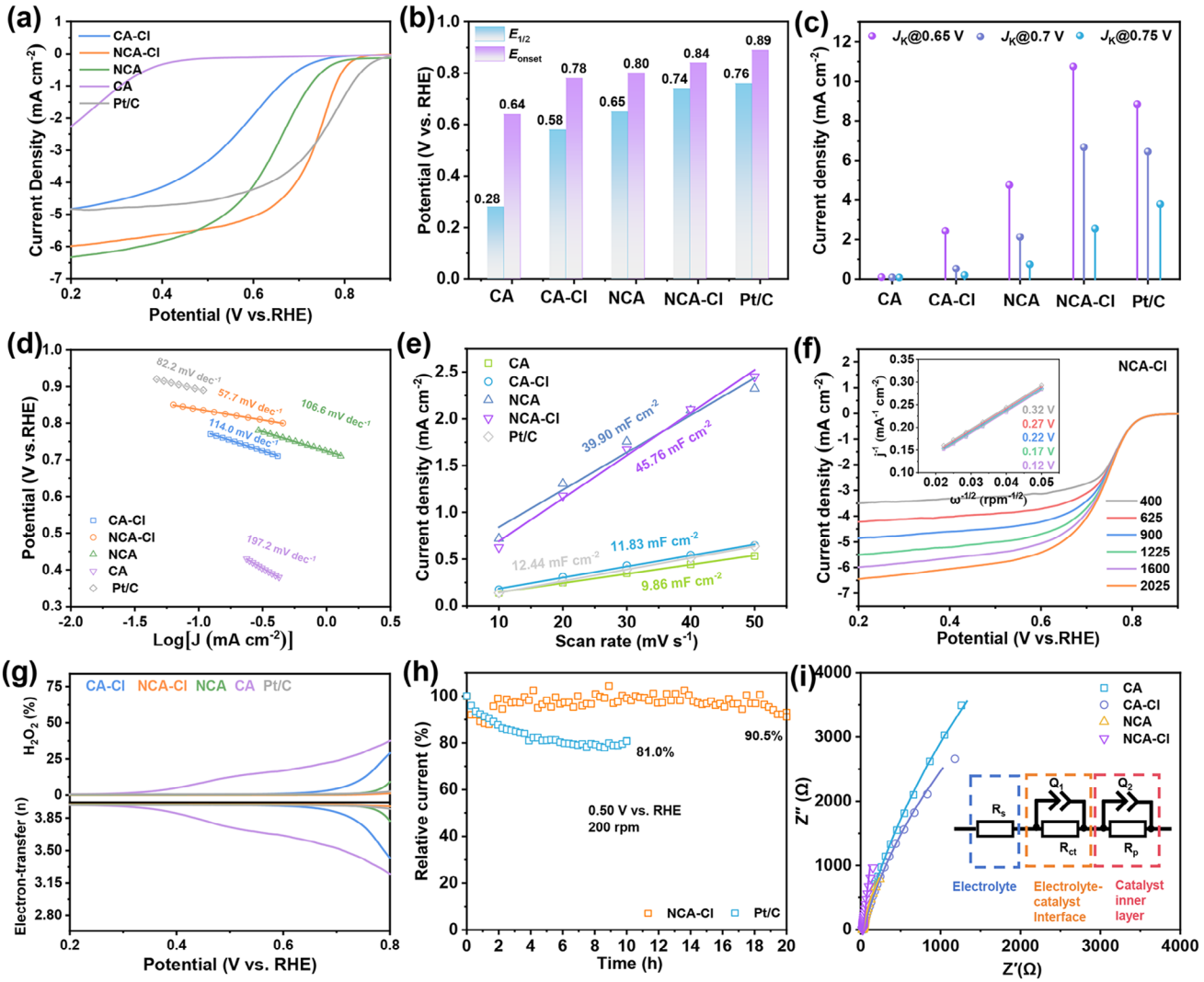


**Figure 4.** ORR activity of NCA-Cl in 0.1 M $HClO_4$. a) LSV patterns. b) $E_{onset}$ and $E_{1/2}$ values. c)$J_K$ values. d) Tafel plots. e) $C_{dl}$ values. f) LSV curves and corresponding *K–L* curves. g) Electron transfer number and $H_2O_2$ peroxide yield. h) The durability of the NCA-Cl catalyst for ORR. i) EIS plots and equivalent circuits.

at 5 mA $cm^{-2}$. When the current density was increased to 10 mA $cm^{-2}$, the capacity still reached 808.1 mAh $g^{-1}$, indicating excellent scalability. The discharge polarization curves of NCA-Cl-based ZABs and commercial Pt/C + $RuO_2$-based ZABs are shown in Figure 5c. Compared with Pt/C+$RuO_2$-based ZABs, NCA-Cl-based ZABs exhibit a lower voltage gap and higher peak power density (206.6 mW $cm^{-2}$), indicating better rechargeability. As displayed in Figure 5d, at 1 mA $cm^{-2}$, the initial voltage gap of the NCA-Cl battery was 0.64 V, with an increase of only 0.03 V during continuous testing up to 400 h, demonstrating stable cycling performance. Due to its high energy and power density, two batteries connected in series can illuminate 38 white lights connected in parallel (as shown in Figure S27, Supporting Information), highlighting its promising potential for practical applications.

The growing demand for wearable electronics has driven the development of flexible energy storage and conversion devices.[25] Compared with aqueous rechargeable ZABs, flexible all-solid-state ZABs are smaller and more suited to the demands of wearable devices. Benefiting from the excellent compression cycling and electrocatalytic performance of the NCA-Cl, NCA-Cl's application was further extended as a cathode air electrode in flexible solid-state ZABs, as shown in Figure 5e. The assembled flexible ZABs demonstrated an open-circuit voltage of 1.45 V and a low charge–discharge voltage gap, as illustrated in Figure S28 (Supporting Information). The maximum power density of the device reached 31.3 mW $cm^{-2}$, as shown in Figure 5F. The discharge voltage plateau is relatively stable at current densities of 1–10 mA $cm^{-2}$, suggesting that the battery retains robust performance, as indicated in Figure 5f. Battery performance was further evaluated under varying bending angles. As shown in Figure 5h, under different bending angles, the charge–discharge curves of the batteries remain identical, and the charge–discharge voltage gap is within 1 V. It was also

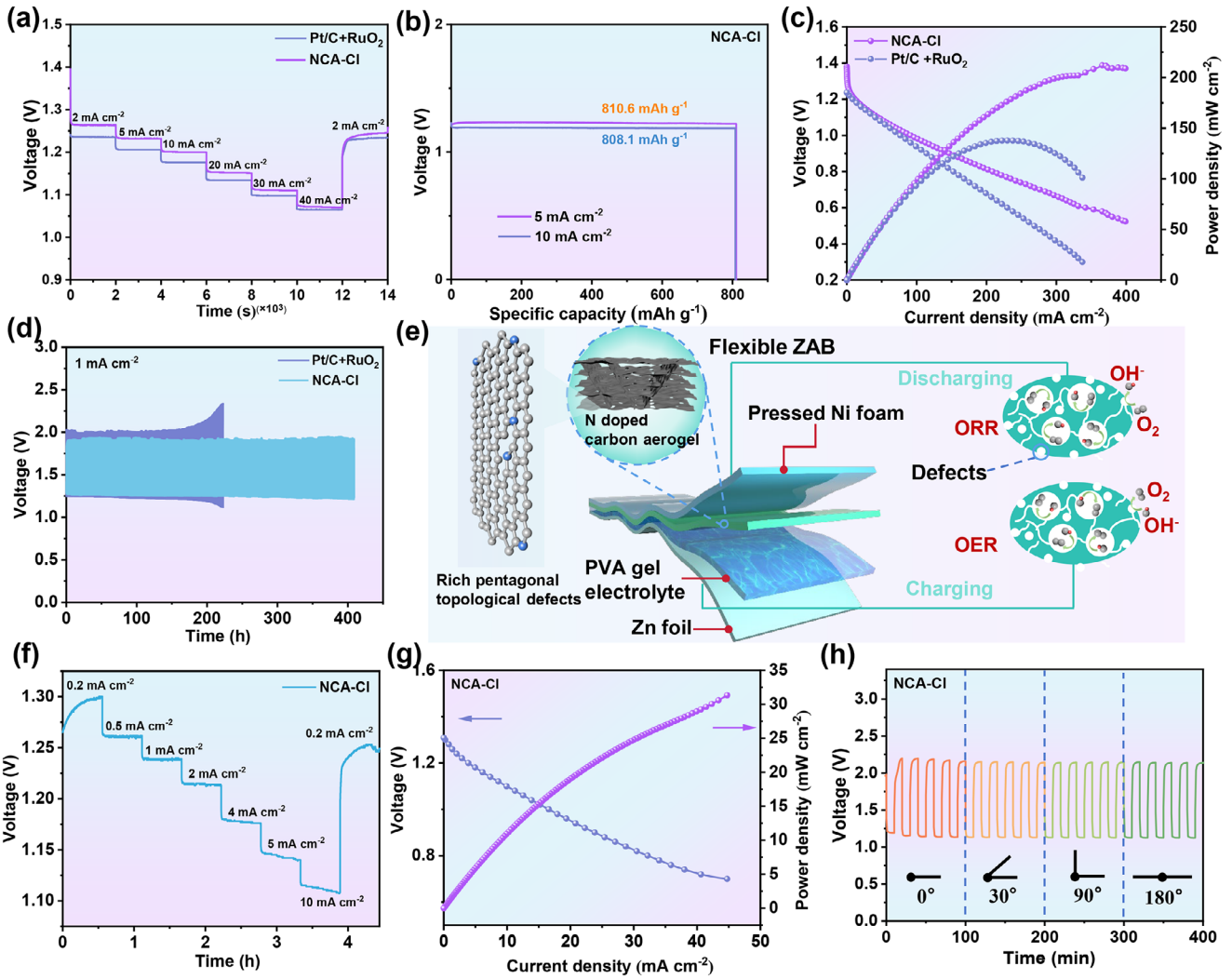


**Figure 5.** Electrochemical performances of the NCA-Cl-based aqueous and compressible flexible ZAB. a) Discharge curves of the NCA-Cl-based and Pt/C+$RuO_2$ ZAB at various current densities. b) Specific discharge capacities at current densities of 5 and 10 mA $cm^{-2}$. c) Power density curves of the rechargeable Zn-air batteries with NCA-Cl-based and Pt/C+$RuO_2$. d) Charge–discharge cycle stability curve at 1.0 mA $cm^{-2}$. e) Schematic illustration of a flexible ZAB using NCA-Cl as the air cathode. f) Discharge curves with current densities from 1 to 10 mA $cm^{-2}$. g) Polarization and power density curves of the rechargeable flexible ZAB with NCA-Cl. h) Charge and discharge cycle tests at different folding angles at 1 mA $cm^{-2}$.

observed that the small fans continued to operate, as shown in Figure S29 (Supporting Information).

### 2.5. Theoretical Investigation

In order to demonstrate that the "desirable" catalyst can facilitate the oxygen reduction reaction (ORR), four models have been established. These are GC (carbon), CN (nitrogen-doped carbon), C-565 (pentagonal defective carbon), and C-565-N (pentagonal defect coupled nitrogen-doped carbon). **Figures** 6a and S20 (Supporting Information) show the partial density of states (pDOS) and charge densities of the four conformations. Compared to the other three conformations, C-565-N shows a higher density of states near the Fermi level, which may lead to the higher catalytic performance of C-565-N.[26] The calculated Bader charges further confirm that C-565-N has a more favorable electronic structure. Carbon loses 0.227 electrons in C-565-N, making C-565-N more favorable for $O_2$ adsorption (Figure 6b).[27] Considering that NCA-Cl prefers 4-electron reactions in electrochemical tests, the corresponding ORR mechanism has two pathways, associative pathway and dissociative pathway. These two pathways can be discriminated by in situ IR detection of the presence of $^*$OOH. Since the pentagonal carbon in the defective carbon is more likely to be the oxygen adsorption site, it can be judged that the oxygen adsorption model is more likely to be the Pauling model, which can still be judged by in situ ATR-SEIRAS. Therefore we first calculated the free energies of adsorption of different intermediates for the four models. The free energy diagrams of the four-electron ORR processes on GC, CN, C-565, and C-565-N are presented in Figure 6c,d and Figure S31 (Supporting Information). The optimized oxygen-containing intermediates ($^*O_2$, $^*$OOH, $^*$O, and $^*$OH) on GC, CN, C-565, and C-565-N in the corresponding configurations are presented in Figures S32–S35

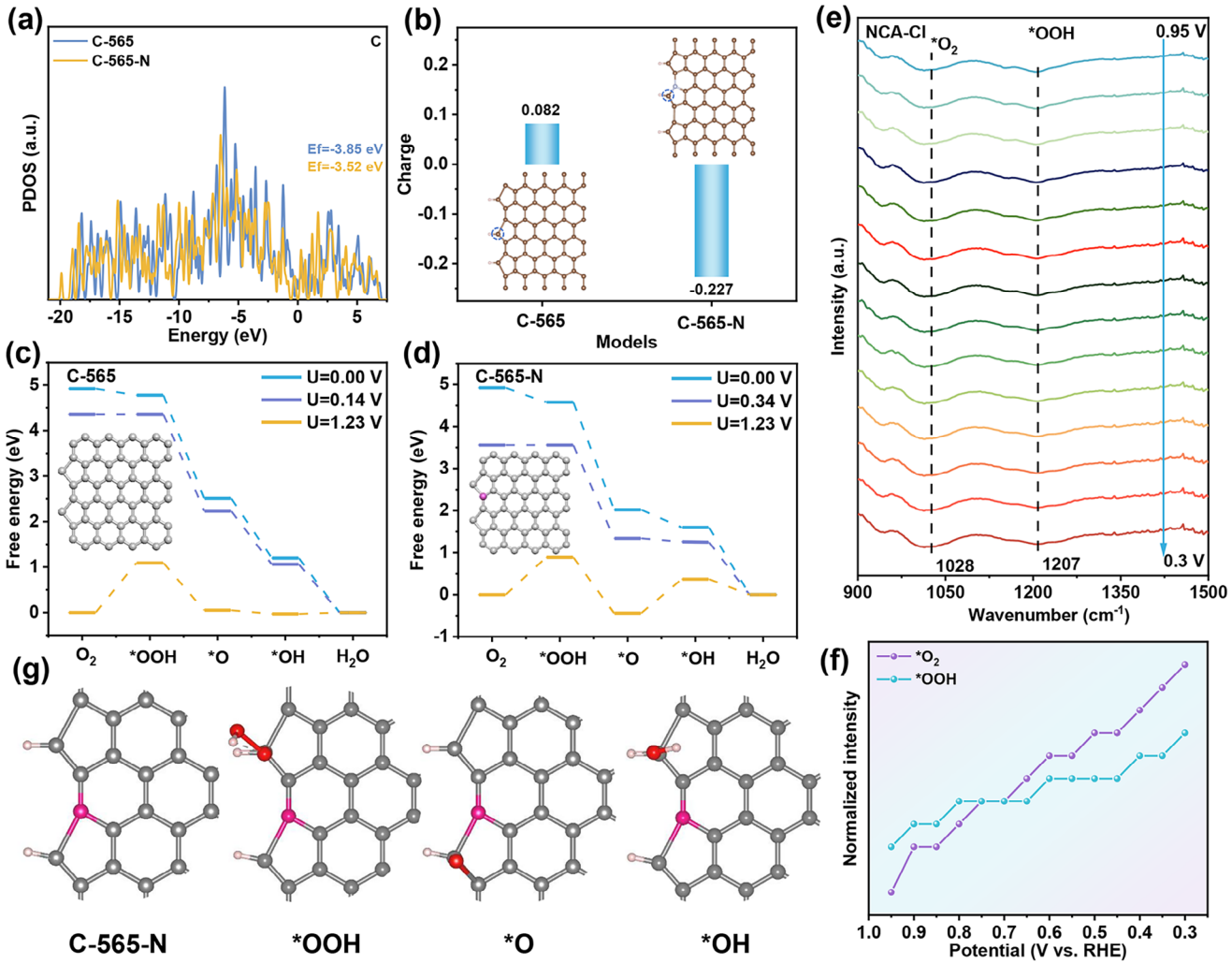


**Figure 6.** Density functional theory calculations. a) The projected density of states (PDOS) and b) Bader charges of C-565 and C-565-N structures. Calculated ORR free energy diagrams of c) C-565, and d) C-565-N. e) In situ FTIR spectra for NCA-Cl in 0.1 M KOH. f) The detailed variations of $^*O_2$ and $^*$OOH with potential. g) Optimized configurations of $^*$, $^*$OOH, $^*$O, and $^*$OH on NCA-Cl.

(Supporting Information). The free energies of GC, CN, C-565, and C-565-N at zero electrode potential demonstrate a downhill energy path, indicating a thermodynamic exothermic process. The theoretical limiting potential of C-565-N (0.34 V) is higher than that of GC (0.20 V), CN (0.28 V), and C-565 (0.14 V), indicating that the activity of C-565-N on ORR was significantly enhanced. At the theoretical equilibrium potential (U = 1.23 V), the reduction of $O_2$ to $^*$OOH by GC, CN, C-565, and C-565-N were all heat-absorbing reactions and were the decisive speed steps for ORR. Among the materials under consideration, C-565-N requires only 0.89 V to convert $O_2$ to $^*$OOH. The pentagonal carbon defects and nitrogen doping act in synergy to enhance the adsorption of $O_2$ and, as a consequence, the ORR performance. The in situ ATR-SEIRAS measurements were performed to identify the vibrational frequencies corresponding to the various intermediates formed during the ORR process (Figure 6e,f). The local coordination structure of NCA-Cl was investigated in oxygen-saturated 0.1 M KOH from 0.95 to 0.3 V. The adsorbed $O_2^-$ on NCA-Cl exhibited an O—O stretching vibrational peak at a wavelength of ≈1027 $cm^{-1}$.[28] The intensity of the peak at 1207 $cm^{-1}$ increased with the decrease of the applied potential, indicating the generation of $^*$OOH intermediates and a four-electronic ORR process on the catalyst surface.[29] Figure 6g illustrates the optimized adsorption configurations of the ORR intermediates ($^*$OOH, $^*$O, and $^*$OH) on NCA-Cl. In conclusion, in situ, ATR-SEIRAS and DFT calculations demonstrate the formation of $^*O_2$ and $^*$OOH reaction intermediate on pentagonal carbon defect sites during the ORR process, as well as high selectivity in the four-electron process.

## 3. Conclusion

In conclusion, nitrogen-doped carbon aerogel electrocatalysts (NCA-Cl) coupled with rich pentagonal defects were prepared for flexible zinc-air batteries using a one-step pyrolysis method. During pyrolysis, nitrogen atoms undergo a dynamic process of capture and collisional uprooting, which induces carbon rearrangement of unsaturated carbon atoms to form pentagonal

defects. The one-piece electrocatalyst, which exhibits a distinctive electronic structure, displayed remarkable electrocatalytic activity and stability in both alkaline ($E_{1/2}$ = 0.89 V vs RHE at 0.1 M KOH) and acid medium ($E_{1/2}$ = 0.74 V vs RHE at 0.1 M $HClO_4$). Theoretical calculations indicate that the high ORR performance of the NCA-Cl catalyst is due to a synergistic effect between the pentagonal defects and the nitrogen dopant, which together modulate the geometrical and electronic properties of the carbon substrate, ensuring the high affinity of the catalyst for $O_2$ as well as the appropriate adsorption/desorption capacity of the key $^*OOH$ intermediates. When employed as a cathode catalyst for aqueous zinc batteries, NCA-Cl exhibited a peak power density of 206.6 mW $cm^{-2}$, a specific capacity of 810.6 mAh $g^{-1}$, and demonstrated stable operation for over 400 h at a current density of 1 mA $cm^{-2}$. Furthermore, flexible zinc-air batteries assembled with NCA-Cl-based catalysts also exhibited remarkable performance. This work not only significantly advances our knowledge of the origin of topological carbon defects, but also offers an effective approach for the controlled synthesis of targeted topological defects in nanocarbon.

## Supporting Information

Supporting Information is available from the Wiley Online Library or from the author.

## Acknowledgements

The authors were grateful for the financial support by the National Key Research and Development Program (Grant No. 2023YFE0109600), National Natural Science Foundation of China (Grant No. 32471811, 32401519, 32201499, 31971614, 52003083, and 32301533), Guangzhou Key Research and Development Program (Grant No. 2023B03J1330), Guangdong Basic and Applied Basic Research Foundation (Grant Nos. 2024A1515011229, 2021A1515110205, 2021A1515110245 and 2023B1515040013), Guangzhou Basic and Applied Basic Research Foundation (Grant Nos. 2024A04J3413 and 2024A04J3704), State Key Laboratory of Pulp and Paper Engineering (Grant Nos. 2023PY01, 2022PY02, and 202215), National Program for Support of Top-notch Young Professionals (Grant No. x2qsA4210090), and China Postdoctoral Science Foundation (Grant Nos. 2023M732021). The authors used the Phychemi Co. Rotating Ring-Disk Electrode (DC-DSR ROTATOR) to test the performance of the catalyst in this experiment. Thanks to eceshi(www.eceshi.com) for the EPR analysis.

## Conflict of Interest

The authors declare no conflict of interest.

## Data Availability Statement

The data that support the findings of this study are available from the corresponding author upon reasonable request.

## Keywords

carbon aerogel, nitrogen-doped, oxygen reduction reaction, topological defects, zinc-air battery

Received: February 17, 2025
Published online: March 16, 2025

[1] a) M. Liu, J. Zhang, H. Su, Y. Jiang, W. Zhou, C. Yang, S. Bo, J. Pan, Q. Liu, *Nat. Commun.* **2024**, *15*, 1675; b) B. Tang, Y. Zhou, Q. Ji, Z. Zhuang, L. Zhang, C. Wang, H. Hu, H. Wang, B. Mei, F. Song, S. Yang, B. M. Weckhuysen, H. Tan, D. Wang, W. Yan, *Nat. Synth.* **2024**, *3*, 878.

[2] a) H. Xia, R. Pang, X. Dong, Q. Liu, J. Chen, E. Wang, J. Li, *J. Am. Chem. Soc.* **2023**, *145*, 25695; b) Z. Huang, M. Li, X. Yang, T. Zhang, X. Wang, W. Song, J. Zhang, H. Wang, Y. Chen, J. Ding, W. Hu, *J. Am. Chem. Soc.* **2024**, *146*, 24842; c) B. Wu, H. Meng, X. Chen, Y. Guo, L. Jiang, X. Shi, J. Zhu, J. Long, W. Gao, F. Zeng, W.-J. Jiang, Y. Zhu, D. Wang, L. Mai, *Angew. Chem., Int. Ed.* **2025**, *64*, 202415071; d) L. Ye, W. Chen, Z.-J. Jiang, Z. Jiang, *Carbon Energy* **2024**, *6*, e457; e) Y. Liu, Z. Jiang, Z.-J. Jiang, *Adv. Funct. Mater.* **2023**, *33*, 2302883; f) Y. Pang, Z. Mo, H. Wang, X. Wang, V. Linkov, R. Wang, *ACS Sustainable Chem. Eng.* **2021**, *9*, 5526; g) Y. Chen, S. Hu, F. Nichols, F. Bridges, S. Kan, T. He, Y. Zhang, S. Chen, *J. Mater. Chem. A* **2020**, *8*, 11649; h) S. Zeng, H. Chen, H. Wang, X. Tong, M. Chen, J. Di, Q. Li, *Small* **2017**, *13*, 1700518.

[3] a) A. Wang, J. Li, T. Zhang, *Nat. Rev. Chem.* **2018**, *2*, 65; b) X. Liang, N. Fu, S. Yao, Z. Li, Y. Li, *J. Am. Chem. Soc.* **2022**, *144*, 18155; c) L. Wang, D. Wang, Y. Li, *Carbon Energy* **2022**, *4*, 1021.

[4] a) G. Wu, P. Zelenay, *Nat. Rev. Mater.* **2024**, *9*, 643; b) S. Liu, C. Li, M. J. Zachman, Y. Zeng, H. Yu, B. Li, M. Wang, J. Braaten, J. Liu, H. M. Meyer, M. Lucero, A. J. Kropf, E. E. Alp, Q. Gong, Q. Shi, Z. Feng, H. Xu, G. Wang, D. J. Myers, J. Xie, D. A. Cullen, S. Litster, G. Wu, *Nat. Energy* **2022**, *7*, 652; c) J. Li, M. Chen, D. A. Cullen, S. Hwang, M. Wang, B. Li, K. Liu, S. Karakalos, M. Lucero, H. Zhang, C. Lei, H. Xu, G. E. Sterbinsky, Z. Feng, D. Su, K. L. More, G. Wang, Z. Wang, G. Wu, *Nat. Catal.* **2018**, *1*, 935.

[5] a) K. Gong, F. Du, Z. Xia, M. Durstock, L. Dai, *Science* **2009**, *323*, 760; b) M. Shao, Q. Chang, J.-P. Dodelet, R. Chenitz, *Chem. Rev.* **2016**, *116*, 3594; c) C. Hu, R. Paul, Q. Dai, L. Dai, *Chem. Soc. Rev.* **2021**, *50*, 11785; d) S. Zaman, L. Huang, A. I. Douka, H. Yang, B. You, B. Y. Xia, *Angew. Chem., Int. Ed.* **2021**, *60*, 17832; e) P. Cui, L. Zhao, Y. Long, L. Dai, C. Hu, *Angew. Chem., Int. Ed.* **2023**, *62*, 202218269; f) R. Paul, L. Zhu, H. Chen, J. Qu, L. Dai, *Adv. Mater.* **2019**, *31*, 1806403; g) Y. Zhao, D. P. Adiyeri Saseendran, C. Huang, C. A. Triana, W. R. Marks, H. Chen, H. Zhao, G. R. Patzke, *Chem. Rev.* **2023**, *123*, 6257.

[6] a) D. Guo, R. Shibuya, C. Akiba, S. Saji, T. Kondo, J. Nakamura, *Science* **2016**, *351*, 361; b) Z. Li, S. Ji, H. Liu, C. Xu, C. Guo, X. Lu, H. Sun, S. Dou, S. Xin, J. H. Horton, C. He, *Adv. Funct. Mater.* **2024**, *34*, 2314444; c) F. Qiang, J. Feng, H. Wang, J. Yu, J. Shi, M. Huang, Z. Shi, S. Liu, P. Li, L. Dong, *ACS Catal.* **2022**, *12*, 4002; d) H. Zhao, Y. Zhang, L. Li, X. Geng, H. Yang, W. Zhou, C. Sun, B. An, *Chin. Chem. Lett.* **2021**, *32*, 140; e) Q. Lu, X. Zou, K. Liao, R. Ran, W. Zhou, M. Ni, Z. Shao, *Carbon Energy* **2020**, *2*, 461; f) Y. Tang, J. Chen, X. Wang, X. Wang, Y. Zhao, Z. Mao, D. Wang, *Electrochim. Acta* **2019**, *324*, 134880; g) S. K. Singh, K. Takeyasu, J. Nakamura, *Adv. Mater.* **2019**, *31*, 1804297; h) X. Peng, L. Zhang, Z. Chen, L. Zhong, D. Zhao, X. Chi, X. Zhao, L. Li, X. Lu, K. Leng, C. Liu, W. Liu, W. Tang, K. P. Loh, *Adv. Mater.* **2019**, *31*, 1900341.

[7] a) Y. Zhang, J. Liu, Y. Xu, C. Xie, S. Wang, X. Yao, *Chem. Soc. Rev.* **2024**, *53*, 10620; b) J. Zhu, S. Mu, *Adv. Funct. Mater.* **2020**, *30*, 2001097; c) X. Wang, Y. Jia, X. Mao, L. Zhang, D. Liu, L. Song, X. Yan, J. Chen, D. Yang, J. Zhou, K. Wang, A. Du, X. Yao, *Chem* **2020**, *6*, 2009; d) Y. Jia, L. Zhang, L. Zhuang, H. Liu, X. Yan, X. Wang, J. Liu, J. Wang, Y. Zheng, Z. Xiao, E. Taran, J. Chen, D. Yang, Z. Zhu, S. Wang, L. Dai, X. Yao, *Nat. Catal.* **2019**, *2*, 688; e) Q. Wu, Y. Jia, Q. Liu, X. Mao, Q. Guo, X. Yan, J. Zhao, F. Liu, A. Du, X. Yao, *Chem* **2022**, *8*, 2715.

[8] a) A. E. Aliev, J. Oh, M. E. Kozlov, A. A. Kuznetsov, S. Fang, A. F. Fonseca, R. Ovalle, M. D. Lima, M. H. Haque, Y. N. Gartstein, M. Zhang, A. A. Zakhidov, R. H. Baughman, *Science* **2009**, *323*, 1575; b) S. Nardecchia, D. Carriazo, M. L. Ferrer, M. C. Gutierrez, F. del Monte, *Chem. Soc. Rev.* **2013**, *42*, 794; c) K. Wu, L. Zhang, Y. Yuan, L. Zhong,

Z. Chen, X. Chi, H. Lu, Z. Chen, R. Zou, T. Li, C. Jiang, Y. Chen, X. Peng, J. Lu, *Adv. Mater.* **2020**, *32*, 2002292.

[9] a) H. Zhuo, Y. Hu, X. Tong, Z. Chen, L. Zhong, H. Lai, L. Liu, S. Jing, Q. Liu, C. Liu, X. Peng, R. Sun, *Adv. Mater.* **2018**, *30*, 1706705; b) H. Liu, T. Xu, C. Cai, K. Liu, W. Liu, M. Zhang, H. Du, C. Si, K. Zhang, *Adv. Funct. Mater.* **2022**, *32*, 2113082; c) H. Lai, Z. Chen, H. Zhuo, Y. Hu, X. Zhao, J. Yi, H. Zheng, G. Shi, Y. Tong, L. Meng, X. Peng, L. Zhong, *Chin. Chem. Lett.* **2024**, *35*, 108331.

[10] K. Wu, L. Zhang, Y. Yuan, L. Zhong, Z. Chen, X. Chi, H. Lu, Z. Chen, R. Zou, T. Li, C. Jiang, Y. Chen, X. Peng, J. Lu, *Adv. Mater.* **2020**, *32*, 2002292.

[11] T. Jiang, Z. Wang, G. Wei, S. Wu, L. Huang, D. Li, X. Ruan, Y. Liu, C. Jiang, F. Ren, *ACS Energy Lett.* **2024**, *9*, 1915.

[12] G. Gan, S. Fan, X. Li, J. Wang, C. Bai, X. Guo, M. Tade, S. Liu, *ACS Catal.* **2021**, *11*, 14284.

[13] F. Zheng, Y. Yang, Q. Chen, *Nat. Commun.* **2014**, *5*, 5261.

[14] R. Daiyan, X. Tan, R. Chen, W. H. Saputera, H. A. Tahini, E. Lovell, Y. H. Ng, S. C. Smith, L. Dai, X. Lu, R. Amal, *ACS Energy Lett.* **2018**, *3*, 2292.

[15] H. Yang, M. Gong, J. Hu, B. Liu, Y. Chen, J. Xiao, S. Li, Z. Dong, H. Chen, *Energy Fuels* **2020**, *34*, 3412.

[16] a) L. Tan, J. Xu, X. Zhang, Z. Hang, Y. Jia, S. Wang, *Appl. Surf. Sci.* **2015**, *356*, 447; b) G. Wang, G. Dai, S. Ding, J. Wu, S. Wang, *J. Anal. Appl. Pyrolysis* **2021**, *156*, 105184.

[17] F. Chen, L.-L. Liu, J.-H. Wu, X.-H. Rui, J.-J. Chen, Y. Yu, *Adv. Mater.* **2022**, *34*, 2202891.

[18] Y. Tian, M. Li, Z. Wu, Q. Sun, D. Yuan, B. Johannessen, L. Xu, Y. Wang, Y. Dou, H. Zhao, S. Zhang, *Angew. Chem., Int. Ed.* **2022**, *61*, 202213296.

[19] D. Chen, K. Cen, X. Zhuang, Z. Gan, J. Zhou, Y. Zhang, H. Zhang, *Combust. Flame* **2022**, *242*, 112142.

[20] H. Jiang, J. Gu, X. Zheng, M. Liu, X. Qiu, L. Wang, W. Li, Z. Chen, X. Ji, J. Li, *Energy Environ. Sci.* **2019**, *12*, 322.

[21] a) D. Xue, Y. Guo, B.-A. Lu, H. Xia, W. Yan, D. Xue, S. Mu, J.-N. Zhang, *Adv. Sci.* **2023**, *10*, 2302930; b) Z. Wu, Y. Yu, G. Zhang, Y. Zhang, R. Guo, L. Li, Y. Zhao, Z. Wang, Y. Shen, G. Shao, *Adv. Sci.* **2022**, *9*, 2200614; c) X. Zheng, Y. Qian, H. Gong, W. Shi, J. Yan, W. Wang, X. Guo, J. Zhang, X. Cao, R. Yang, *Appl. Catal., B* **2022**, *319*, 121937; d) Y. Wang, N. Xu, R. He, L. Peng, D. Cai, J. Qiao, *Appl. Catal. B* **2021**, *285*, 119811; e) C. Liu, F. Liu, H. Li, J. Chen, J. Fei, Z. Yu, Z. Yuan, C. Wang, H. Zheng, Z. Liu, M. Xu, G. Henkelman, L. Wei, Y. Chen, *ACS Nano* **2021**, *15*, 3309; f) Z. Chen, X. Peng, Z. Chen, T. Li, R. Zou, G. Shi, Y. Huang, P. Cui, J. Yu, Y. Chen, X. Chi, K. P. Loh, Z. Liu, X. Li, L. Zhong, J. Lu, *Adv. Mater.* **2023**, *35*, 2209948; g) L. Zhong, C. Jiang, M. Zheng, X. Peng, T. Liu, S. Xi, X. Chi, Q. Zhang, L. Gu, S. Zhang, G. Shi, L. Zhang, K. Wu, Z. Chen, T. Li, M. Dahbi, J. Alami, K. Amine, J. Lu, *ACS Energy Lett.* **2021**, *6*, 3624; h) K. Cui, Q. Wang, Z. Bian, G. Wang, Y. Xu, *Adv. Energy Mater.* **2021**, *11*, 2102062.

[22] Z. Wang, X. Jin, C. Zhu, Y. Liu, H. Tan, R. Ku, Y. Zhang, L. Zhou, Z. Liu, S.-J. Hwang, H. J. Fan, *Adv. Mater.* **2021**, *33*, 2104718.

[23] T. Li, Y. Liu, Y. Huang, L. Zhang, Z. Chen, W. Yang, G. Shi, J. Zhou, R. Zou, J. Gan, L. Zhong, X. Peng, *Small* **2024**, *20*, 2311675.

[24] a) P. Sabhapathy, P. Raghunath, A. Sabbah, I. Shown, K. S. Bayikadi, R.-K. Xie, V. Krishnamoorthy, M.-C. Lin, K.-H. Chen, L.-C. Chen, *Small* **2023**, *19*, 2303598; b) R. K. Singh, R. Devivaraprasad, T. Kar, A. Chakraborty, M. Neergat, *J. Electrochem. Soc.* **2015**, *162*, F489.

[25] a) T. Li, X. Peng, P. Cui, G. Shi, W. Yang, Z. Chen, Y. Huang, Y. Chen, J. Peng, R. Zou, X. Zeng, J. Yu, J. Gan, Z. Mu, Y. Chen, J. Zeng, J. Liu, Y. Yang, Y. Wei, J. Lu, *SmartMat* **2021**, *2*, 519; b) W. Yang, W. Yang, J. Zeng, Y. Chen, Y. Huang, J. Liu, J. Gan, T. Li, H. Zhang, L. Zhong, X. Peng, *Prog. Mater. Sci.* **2024**, *144*, 101264; c) Y. Zhang, D. Wu, F. Huang, Y. Cai, Y. Li, H. Ke, P. Lv, Q. Wei, *Adv. Funct. Mater.* **2022**, *32*, 2203204.

[26] S. Wu, X. Liu, H. Mao, J. Zhu, G. Zhou, J. Chi, Z. Wu, L. Wang, *Adv. Energy Mater.* **2024**, *14*, 2400183.

[27] F. Kong, X. Cui, Y. Huang, H. Yao, Y. Chen, H. Tian, G. Meng, C. Chen, Z. Chang, J. Shi, *Angew. Chem., Int. Ed.* **2022**, *61*, 202116290.

[28] S. Huang, D. Tranca, F. Rodríguez-Hernández, J. Zhang, C. Lu, J. Zhu, H.-W. Liang, X. Zhuang, *Angew. Chem., Int. Ed.* **2024**, *63*, 202314833.

[29] S. Mondal, D. Bagchi, M. Riyaz, S. Sarkar, A. K. Singh, C. P. Vinod, S. C. Peter, *J. Am. Chem. Soc.* **2022**, *144*, 11859.